Catch Me if You Can: Biased Distribution of Lyα-emitting Galaxies according to the Viewing Direction

Rieko Momose[1] , Kazuhiro Shimasaku[1,2] , Kentaro Nagamine[3,4,5] , Ikkoh Shimizu[6], Nobunari Kashikawa[1,2] ,
Makoto Ando[1], and Haruka Kusakabe[7]

[1] Department of Astronomy, School of Science, The University of Tokyo, 7-3-1 Hongo, Bunkyo-ku, Tokyo 113-0033, Japan; momose@astron.s.u-tokyo.ac.jp
[2] Research Center for the Early Universe, The University of Tokyo, 7-3-1 Hongo, Bunkyo-ku, Tokyo 113-0033, Japan
[3] Department of Earth and Space Science, Osaka University, 1-1 Machikaneyama, Toyonaka, Osaka 560-0043, Japan
[4] Department of Physics and Astronomy, University of Nevada, Las Vegas, NV 89154-4002, USA
[5] Kavli-IPMU (WPI), The University of Tokyo, 5-1-5 Kashiwanoha, Kashiwa, Chiba 277-8583, Japan
[6] Shikoku Gakuin University, 3-2-1 Bunkyocho, Zentsuji, Kagawa 765-0013, Japan
[7] Observatoire de Genève, Université de Genève, 51 chemin de Pégase, 1290 Versoix, Switzerland

Abstract

We report that Lyα-emitting galaxies (LAEs) may not faithfully trace the cosmic web of neutral hydrogen (H I), but their distribution is likely biased depending on the viewing direction. We calculate the cross-correlation function (CCF) between galaxies and Lyα forest transmission fluctuations on the near and far sides of the galaxies separately, for three galaxy samples at $z \sim 2$: LAEs, [O III] emitters (O3Es), and continuum-selected galaxies. We find that only LAEs have anisotropic CCFs, with the near side one showing lower signals up to $r = 3$–$4\,h^{-1}$ comoving Mpc. This means that the average H I density on the near side of LAEs is lower than that on the far side by a factor of 2.1 under the fluctuating Gunn–Peterson approximation. Mock LAEs created by assigning Lyα equivalent width ($EW_{\mathrm{Ly}\alpha}^{\mathrm{obs}}$) values to O3Es with an empirical relation also show similar, anisotropic CCFs if we use only objects with higher $EW_{\mathrm{Ly}\alpha}^{\mathrm{obs}}$ than a certain threshold. These results indicate that galaxies on the far side of a dense region are more difficult to be detected ("hidden") in Lyα because Lyα emission toward us is absorbed by dense neutral hydrogen. If the same region is viewed from a different direction, a different set of LAEs will be selected as if galaxies are playing hide-and-seek using H I gas. Care is needed when using LAEs to search for overdensities.

Unified Astronomy Thesaurus concepts: Intergalactic medium (813); Galaxy evolution (594); Large-scale structure of the universe (902); Lyman alpha forest (980); Lyman-alpha galaxies (978)

1. Introduction

Matter in the universe is not uniformly distributed in space but forms large-scale filamentary structure or the cosmic web. Many galaxy redshift surveys have depicted the cosmic web of the present-day universe (e.g., de Lapparent et al. 1986; Tegmark et al. 2004; Guzzo et al. 2014; Libeskind et al. 2018). For the young universe, the most successfully used galaxies to map the web are those with hydrogen Lyα emission at 1216 Å (Lyα-emitting galaxies, LAEs). LAEs are one of the major galaxy populations in the young universe (e.g., Hu et al. 1998; Malhotra & Rhoads 2004; Shibuya et al. 2018). LAEs in the post-reionization epoch ($z \leqslant 6$) can be easily detected by narrowband imaging whose wavelength is tuned to Lyα emission at the target redshift. Many LAE surveys have revealed filamentary structures and protoclusters in the young universe (e.g., Shimasaku et al. 2003, 2004; Cai et al. 2017).

However, several studies have recently pointed out that the density peak of LAEs' distribution does not always match that traced by other galaxy populations. For instance, Shimakawa et al. (2017) have found a few megaparsec (Mpc) deviation of LAEs' density peak in a $z = 2$ protocluster from that of Hα-emitting galaxies, which are normal star-forming galaxies commonly seen at high redshifts. A similar offset from continuum-selected galaxies has also been reported (Overzier et al. 2008; Toshikawa et al. 2016; Shi et al. 2019). More

importantly, Momose et al. (2021) have suggested that the peak of LAEs' distribution does not match that of intergalactic medium neutral hydrogen (IGM H I). With its density increasing with matter density, IGM H I is a faithful tracer of the cosmic web that has recently come into use, although the areas mapped by IGM H I are still limited because the observations are very time consuming. These reported discrepancies might imply that LAEs intrinsically avoid dense parts of the cosmic web for some reason (e.g., Shimakawa et al. 2017; Oteo et al. 2018; Shi et al. 2019; Momose et al. 2021).

Alternatively, the discrepancies may be a bias caused by the absorption of Lyα photons by IGM H I in dense regions (e.g., Dijkstra et al. 2007; Laursen et al. 2011; Zheng et al. 2011; Gurung-López et al. 2020; Hayes et al. 2021). In this case, a biased distribution of LAEs along the line of sight is expected. LAEs located on the far side of a dense region are more difficult to detect because their Lyα emission toward us is heavily absorbed by IGM H I during passing through the region (Zheng et al. 2011; Gurung-López et al. 2020). As a result, fewer LAEs will be detected on the far side even if the original number is identical. So far, however, no observation has reported such an anisotropic distribution.

Aiming at finding such anisotropic features, we investigate the connection between LAEs and IGM H I with a publicly available 3D IGM tomography map of the Lyα forest transmission fluctuation (δ_F), called the COSMOS Lyα Mapping And Tomography Observations (CLAMATO; Lee et al. 2016, 2018), as an extension of Momose et al. (2021). This Letter is organized as follows. We introduce the data and

1) CCF

2) 1D-CCF along the line-of-sight

3) 1D-CCF along transverse directions
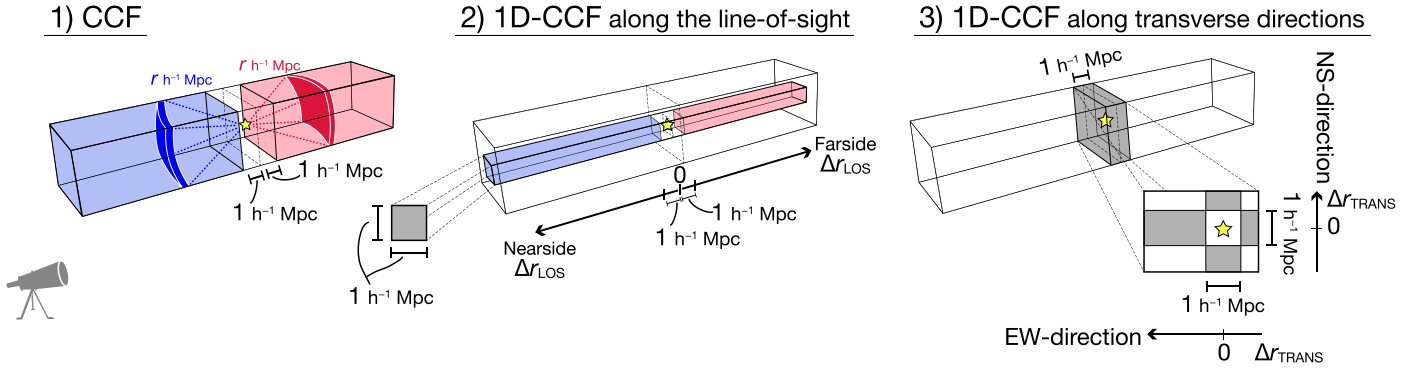
Figure 1. Schematic diagrams of the CLAMATO data used in each analysis. The CCF and the 1D-CCFs along the line-of-sight and transverse directions are displayed from left to right. Note that the CLAMATO spans comoving dimensions of $(x, y, z) = (30, 24, 438)\ h^{-1}$ cMpc. The subvolume of the CLAMATO used in each analysis is colored in light blue (near side), faint red (far side), and gray (two transverse directions). The exact area used to calculate the CCF at radius r is colored in dark blue and dark red for the near and far sides, respectively.

methodology used in this study in Section 2 and present the results in Section 3. An examination of cross-correlation functions (CCFs) using mock LAEs is presented in Section 4. We summarize our study together with discussions in Section 5. We use a cosmological parameter set of $(\Omega_m, \Omega_\Lambda, h) = (0.31, 0.69, 0.7)$ throughout this Letter (Lee et al. 2016, 2018). All distances are described in a comoving unit unless otherwise stated. We indicate "cosmic web" and "IGM" as those traced by H I unless otherwise specified.

2. Data and Analyses

2.1. IGM H I Data

We use the CLAMATO[8] as a tracer of IGM H I (Lee et al. 2016, 2018) . The CLAMATO is a 3D data cube of δ_F over $z = 2.05$–2.55, which is reconstructed from 240 galaxies and quasars spectra taken by the LRIS on the Keck I (Oke et al. 1995; Steidel et al. 2004). Here, δ_F is defined by

$$\delta_F = \frac{F}{\langle F_z \rangle} - 1, \qquad (1)$$

where F and $\langle F_z \rangle$ are the Lyα forest transmission and its cosmic mean from Faucher-Giguère et al. (2008). Hence, δ_F is the excess transmission to Lyα photons. Higher IGM H I densities give lower F, and negative (positive) $\delta_F(x)$ values indicate higher (lower) H I densities than the cosmic mean. The effective transverse separation of the CLAMATO is 2.04 comoving h^{-1} Mpc (hereafter h^{-1} cMpc). The spatial resolution in the line-of-sight direction is $2.35\ h^{-1}$ cMpc at $z = 2.3$. The final 3D data cube of the CLAMATO spans $(x, y, z) = (30, 24, 438)\ h^{-1}$ cMpc with $0.5\ h^{-1}$ cMpc pixel size.

2.2. Galaxy Samples

We use three galaxy samples constructed in Momose et al. (2021). One is a sample of 19 LAEs whose redshifts have been determined by nebular lines of Hα and/or [O III][9] (Nakajima et al. 2012, 2013; Hashimoto et al. 2013; Shibuya et al. 2014; Konno et al. 2016). The other two used as control samples are 85 [O III]λλ4959, 5007 emitting galaxies (O3Es), and 570 continuum-selected galaxies with a spectroscopic redshift. O3Es and

continuum-selected galaxies are also star-forming galaxies like LAEs, but their selections, based on [O III] and far-ultraviolet luminosities, respectively, are not affected by IGM H I.

2.3. Analyses

We conduct two different analyses. The first is the CCF between galaxies and the CLAMATO using the same definition of our previous work (Momose et al. 2021):

$$\xi_{\delta F}(r) = \frac{1}{\sum_{i=1}^{N(r)} \omega_{F,i}} \sum_{i=1}^{N(r)} \omega_{F,i} \delta_{F,i}$$
$$- \frac{1}{\sum_{j=1}^{M(r)} \omega_{ran,j}} \sum_{j=1}^{M(r)} \omega_{ran,j} \delta_{ran,j}, \qquad (2)$$

$$\omega_{F,i} = \frac{1}{(\sigma_{F,i})^2}, \quad \omega_{ran,j} = \frac{1}{(\sigma_{ran,j})^2}, \qquad (3)$$

where $\xi_{\delta F}$ is the cross-correlation at a separation r; $\delta_{F,i}$ and $\delta_{ran,j}$ are the transmission fluctuation at places i and j separated by r from a galaxy and random point, respectively, in question with $\sigma_{F,i}$ and $\sigma_{ran,j}$ being their errors; $N(r)$ and $M(r)$ represent the numbers of pixel-galaxy and pixel-random pairs with separation r, respectively. The σ_F and σ_{ran} are evaluated with the CLAMATO's 3D noise standard deviation measurements, including pixel noise, finite skewer sampling, and the intrinsic variance of the Lyα forest (Lee et al. 2018). Unlike our previous studies (Momose et al. 2021), we calculate the CCFs on the near and far sides of galaxies separately. The CCF on the near (far) side is derived only using the data in the near (far) hemispheres (regions colored in blue and red of Figure 1, left). For both calculations, the data within a line-of-sight separation of $1\ h^{-1}$ cMpc from each galaxy is excluded to eliminate the influence of H I in the circumgalactic medium (CGM).

The second analysis is to compute a one-dimensional CCF (hereafter "1D-CCF") defined by

$$\langle \delta_F \rangle(\Delta r) = \frac{1}{\sum_{i=1}^{N(\Delta r)} \omega_{F,i}} \sum_{i=1}^{N(\Delta r)} \omega_{F,i} \delta_{F,i}, \qquad (4)$$

for the line-of-sight and two transverse directions. For the line-of-sight direction, we use narrow tomography data of the projected $1 \times 1\ (h^{-1}$ cMpc$)^2$ area centered at individual galaxies

---

[8]   The data are from http://clamato.lbl.gov.
[9]   Although some of the LAEs are also bright in [O III] emission, we refer to them as LAEs based on their first identification from narrowband images.
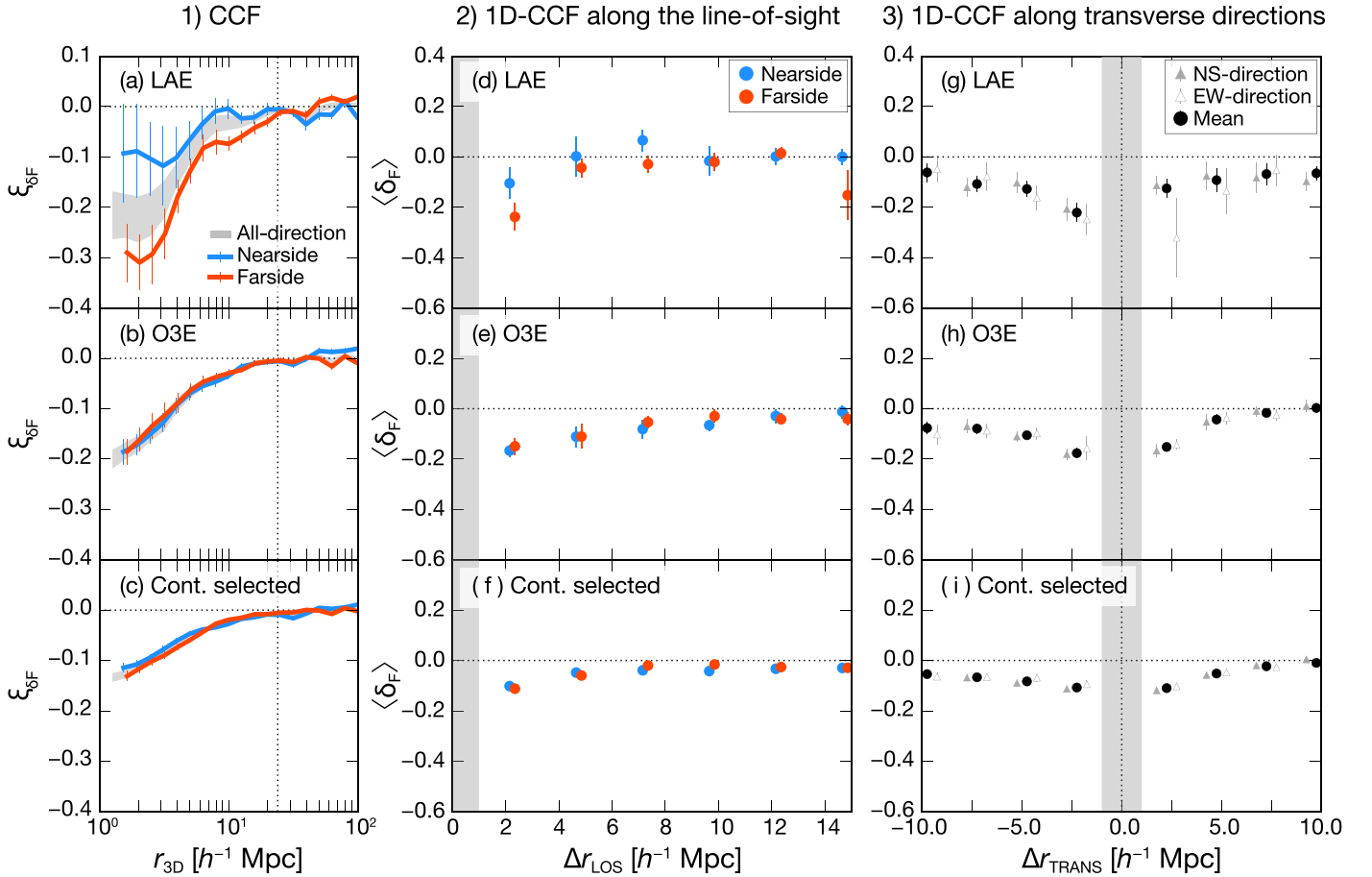
Figure 2. CCF (panels (a)–(c)) and 1D-CCFs along the line-of-sight (panels (d)–(f)) and two transverse directions (panels (g)–(i)) for LAEs, O3Es, and continuum-selected galaxies. Panels (a)–(c): blue and red lines indicate, respectively, the CCFs on the near and far sides of galaxies. Gray shades represent the CCFs calculated using all directions (Momose et al. 2021). A vertical dotted line indicates the possible largest radius for 3D cross-correlation calculations. Panels (d)–(f): $\langle \delta_F \rangle$ along the line-of-sight direction in $2.5\,h^{-1}$ cMpc steps over $1 \leqslant (\Delta r/h^{-1}$ cMpc$) \leqslant 16$, plotted against the absolute distance from galaxies Δr_{LOS}, with blue (red) color indicating the near (far) side of them. A gray zone indicates the distance range excluded from the analysis. Panels (g)–(i): $\langle \delta_F \rangle$ along two transverse directions in $2.5\,h^{-1}$ cMpc steps over $-11 \leqslant (\Delta r/h^{-1}$ cMpc$) \leqslant 11$, except the range in $-1 \leqslant (\Delta r/h^{-1}$ cMpc$) \leqslant 1$, where $\Delta r_{\mathrm{TRANS}}$ indicates the distance from galaxies shown in Figure 1 (right). Filled and open triangles denote $\langle \delta_F \rangle$ of the NS and EW directions, respectively, while filled circles indicate the average of the two directions.

(Figure 1, middle). Note that regions colored in light blue and red are referred to as the near and far sides. Similarly, for the transverse directions, we use narrow data of a cross-section of $1 \times 1\ (h^{-1}$ cMpc$)^2$ along with the north–south (NS) and east–west (EW) directions (Figure 1, right). We measure $\langle \delta_F \rangle (\Delta r)$ in $2.5\,h^{-1}$ cMpc steps over $-16 \leqslant (\Delta r/h^{-1}$ cMpc$) \leqslant 16$ for the line-of-sight direction and $-11 \leqslant (\Delta r/h^{-1}$ cMpc$) \leqslant 11$ for the transverse directions, excluding $-1 \leqslant (\Delta r/h^{-1}$ cMpc$) \leqslant 1$.

In both analyses, errors are estimated with Jackknife resampling by removing one object. Therefore, the number of Jackknife samples is the same as that of galaxies in the original sample. Although Jackknife resampling for the cross-correlation is usually evaluated by dividing the survey volume into several small subvolumes, to be conservative, we do not use this resampling in this study because it gives smaller errors than obtained above (Momose et al. 2021).

3. Results

The results of the two analyses are shown in Figure 2. Figure 2(a) shows that the near side CCF of LAEs is consistently higher than the far side one up to $r = 3 - 4\,h^{-1}$ cMpc, possibly

up to $r \sim 20\,h^{-1}$ cMpc, meaning that the average density of IGM H I gas around LAEs is systematically lower on the near side. The IGM H I density at $3\,h^{-1}$ cMpc between the two sides differs by a factor of 2.1 under the fluctuating Gunn–Peterson approximation (Appendix). In contrast, no such systematic difference is seen in the other two galaxy populations (Figures 2(b) and (c)).

A similar trend is found in the 1D-CCF along the line of sight in Figures 2(d)–(f). Although the difference is marginal, the 1D-CCF of LAEs is higher on the near side up to $\sim 8\,h^{-1}$ cMpc. In contrast, the 1D-CCFs of O3Es and continuum-selected galaxies are nearly symmetric around $\Delta r = 0$, indicating an isotropic H I density distribution along the line of sight with respect to the position of those galaxies. Unlike the 1D-CCF along the line of sight, those along transverse directions (Figures 2(g)–(i)) show nearly symmetric distributions within the 1σ errors with a negative peak at $r = 0$, indicating an isotropic H I density distribution.

We calculate the probability of an anisotropic CCF and 1D-CCF along the line of sight like those seen in LAEs being caused by chance due to a small sample, by conducting the same analyses to randomly selected 19 continuum-selected galaxies and O3Es. The probability is found to be only 2% even if we

loosen the criteria for anisotropy.[10] Therefore, the anisotropy of the H I density found for LAEs is unlikely to be by chance.

One may be concerned that the limited spatial distribution of our LAEs along the transverse directions ((Δx, Δy) = (30, 24) h^{-1} cMpc) and along the line of sight ($z = 2.14$–2.22[11] or 69.7 h^{-1} cMpc) causes an anisotropic H I density distribution along the line of sight. We also conduct the same analyses to 17 O3Es and 108 continuum-selected galaxies in this redshift range and find anisotropy in the CCF and 1D-CCF along the line of sight around O3Es, but with an opposite sign to that of LAEs: the H I density is lower on the far side than on the near side. Besides, the probability that randomly selected galaxies reproduce an anisotropic CCF and 1D-CCF along the line of sight like those found for real LAEs is less than 1%. These results indicate that the anisotropy seen around LAEs is unlikely to be due to a small sample in a limited redshift range.

4. A Toy Model with Mock Lyα-emitting Galaxies

We show in Section 3 that the IGM H I density distribution around LAEs is anisotropic, with the density on the near side being lower than on the far side. Considering that the H I density averaged over all directions decreases with the distance from LAEs, this result leads to the picture that LAEs for a given dense region are preferentially distributed on its near side; at any position on the near side, the H I gas in front of that position should be more transparent to Lyα than on the opposite side.

The most natural explanation of this anisotropy is a selection effect. LAEs on the far side of dense regions are more difficult to detect because Lyα photons emitted from them toward us have to pass through the dense regions of low Lyα transmission. To test this hypothesis, we construct a toy model with mock LAEs and examine if galaxies, whose intrinsic distribution is normal, show an anisotropic H I density distribution like actual LAEs if the sample is limited to those with strong Lyα emission in the observed-frame owing to their location relative to a dense region.

4.1. Methodology

Our toy model is based on a mock LAE sample created from the O3Es. We carry out the examination as follows. First, we assign each object of the O3E sample an "intrinsic" equivalent width, $EW_{Ly\alpha}^{int}$ (hence an "intrinsic" Lyα luminosity) according to an empirical $EW_{Ly\alpha}$–stellar mass ($M_\star$) relation by Cullen et al. (2020):

$$EW_{Ly\alpha}^{int} = -\frac{0.24 \log M_\star - 4.65}{0.015}. \qquad (5)$$

We use $M_\star$ estimates in the photometric redshift catalog of Straatman et al. (2016). Note that we adopt not the best-fit relation of Cullen et al. (2020) but its upper 1σ envelope because the best-fit relation assigns a large fraction of the

sample negative $EW_{Ly\alpha}^{int}$,[12] which cannot be used for selecting mock LAEs. Nonetheless, this prescription is consistent with the fact that the Lyα luminosities of LAEs are boosted compared with other star-forming galaxies.

Next, we attenuate the Lyα luminosity of each object using the actual line of sight δ_F at the position of this object to obtain an "observed" equivalent width ($EW_{Ly\alpha}^{obs}$) by taking the attenuation by the IGM into account:

$$EW_{Ly\alpha}^{obs} = 0.24 \, EW_{Ly\alpha}^{int} \, \langle F \rangle_{near}^{LOS} + 0.76 \, EW_{Ly\alpha}^{int}, \qquad (6)$$

where $\langle F \rangle_{near}^{LOS}$ is the transmission in the line-of-sight direction averaged over $-5.0 \leqslant (\Delta r / h^{-1}$ cMpc$) \leqslant -1.7$ on the near side, in a projected square of 1×1 (h^{-1} cMpc)^2 area center at the galaxy. Equation (6) comes from the following consideration. First, we assume a double-peaked Lyα profile where the red peak is located 200 km s^{-1} redward of λ(Lyα) while the blue peak, contributing 24% of the total Lyα emission, is centered at -200 km s^{-1} with a 200 km s^{-1} width. This profile is based on a stacked Lyα spectrum of $z = 2.2$ LAEs presented in Matthee et al. (2021) but also roughly consistent with other observations of individual LAEs (e.g., Rakic et al. 2011; Hashimoto et al. 2013, 2015). We then assume that only the blue peak is subject to the IGM attenuation, neglecting the effect of the peculiar motion of galaxies relative to the IGM. Because Lyα photons in the blue peak, which have relative velocities of -300 to -100 km s^{-1}, are redshifted to λ(Lyα) after traveling over $1.7 \leqslant \Delta r / h^{-1}$cMpc $\leqslant 5.1$, we use the line-of-sight transmission averaged over this distance range, $\langle F \rangle_{near}^{LOS}$. We calculate $\langle F \rangle_{near}^{LOS}$ from the excess transmission averaged over the same distance range, $\langle \delta_F \rangle_{near}^{LOS}$, by

$$\langle F \rangle_{near}^{LOS} = (1 + \langle \delta_F \rangle_{near}^{LOS}) \langle F_z \rangle. \qquad (7)$$

We assume $\langle F \rangle_{near}^{LOS} = 1$ for four O3Es whose $\langle F \rangle_{near}^{LOS}$ is larger than unity so that their $EW_{Ly\alpha}^{obs}$ is equal to $EW_{Ly\alpha}^{int}$. We should also note that an observed Lyα luminosity is determined not only by the line-of-sight IGM H I absorption but to some degree by the absorption in all other directions, as pointed out by Zheng et al. (2011). However, since it is extremely complicated to evaluate the impact of Lyα suppression in all directions, we consider the line-of-sight direction alone.

The resultant $EW_{Ly\alpha}^{obs}$ estimates, presented by black circles in Figure 3, are lower than those of actual LAEs plotted as red stars. It is probably because LAEs generally have higher Lyα ISM/CGM escape fractions than continuum and nebular emission line selected galaxies, owing to their lower dust extinction (e.g., Stark et al. 2010; Wardlow et al. 2014; Kusakabe et al. 2015), lower H I column density of the ISM (e.g., Hashimoto et al. 2015), and/or higher ionization parameter (e.g., Nakajima & Ouchi 2014; Sobral et al. 2018). However, our goal here is not to accurately reproduce observed LAEs but to create mock galaxies whose $EW_{Ly\alpha}^{obs}$ are sufficiently widely scattered around the selection threshold, to examine if the selection effect can cause anisotropy in the IGM density similar to the observed one.

---

[10] We set two criteria. The first is that the near side CCF is higher than the far side one beyond the error bars at any radius up to $r = 4 \ h^{-1}$ cMpc. The second criterion is the same as the first one except for the innermost radius by considering the case in mock LAEs presented in Section 4.2. The probability of satisfying each criterion is 0% and 2% (1% and 2%) for continuum-selected galaxies (O3Es).

[11] This redshift range is defined by the FWHM of the narrowband filter used for our LAE search (Nakajima et al. 2012; Konno et al. 2016).

---

[12] We also note that although we regard $EW_{Ly\alpha}$ in the relation as an "intrinsic equivalent width ($EW_{Ly\alpha}^{int}$)" after absorption by the interstellar medium (ISM) and the CGM, it may also be affected by the IGM attenuation.
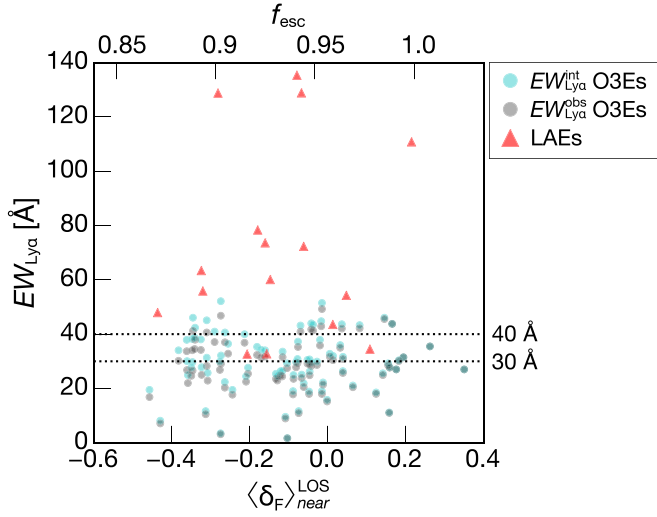
Figure 3. $EW_{Ly\alpha}$ as a function of $\langle\delta_F\rangle$ on the near side over $-5.0 \leqslant (\Delta r/h^{-1} \, \text{cMpc}) \leqslant -1.7$ along the line-of-sight direction, which we refer to as $\langle\delta_F\rangle_{near}^{LOS}$. Cyan and black circles represent, respectively, $EW_{Ly\alpha}^{int}$ and $EW_{Ly\alpha}^{obs}$ of O3Es used to create mock LAEs. The observed $EW_{Ly\alpha}$ of our LAEs are also plotted as filled triangles except for three objects with $EW_{Ly\alpha}^{obs} > 140$ Å. Dashed lines show the two thresholds for selecting mock LAEs. The escape fraction of $Ly\alpha$ photons through the IGM is calculated as $f_{esc} = EW_{Ly\alpha}^{obs}/EW_{Ly\alpha}^{int}$.

Finally, by dropping objects whose $EW_{Ly\alpha}^{obs}$ is below some threshold, we obtain a sample of mock LAEs. We try two threshold $EW_{Ly\alpha}^{obs}$ values. One is 30 Å that is actually adopted to select the $z = 2.2$ LAEs. The other is 40 Å; we try this slightly higher threshold to evaluate how sensitive the results are to the threshold. We select 35 (12) O3Es with $EW_{Ly\alpha}^{obs} \geqslant 30$ (40) Å as mock LAEs. Using those mock LAEs, we conduct the same analyses (CCF and 1D-CCF) as for the real galaxies.

4.2. Results

Figure 4 presents the results of the toy model. A similar trend to that of real LAEs is seen in the $EW_{Ly\alpha}^{obs} \geqslant 40$ Å sample, whose CCF is lower on the far side up to $r = 5 \, h^{-1} \, \text{cMpc}$, implying a factor 1.5 density difference within $r = 3 \, h^{-1} \, \text{cMpc}$ with the FGPA. The 1D-CCF along the line of sight of this sample is also systematically lower on the far side over $|\Delta r_{TRANS}| < 6 \, h^{-1} \, \text{cMpc}$ (Figure 4(d)) in contrast to those along transverse directions, which are nearly symmetric over a similar distance (Figure 4(f)). On the other hand, the $EW_{Ly\alpha}^{obs} \geqslant 30$ Å sample does not show significant line-of-sight anisotropy. We note anisotropy of the 1D-CCFs along transverse directions seen beyond $|\Delta r_{TRANS}| \geqslant 5 \, h^{-1} \, \text{cMpc}$ in Figures 4(e) and (f). This could be due to the small sample size of mock LAEs because the anisotropic feature becomes weaker with increasing sample size, probably by mitigating the large-scale variation in the IGM H I distribution around them.

Interestingly, the degree of anisotropy is sensitive to the threshold $EW_{Ly\alpha}^{obs}$ value. The absence of anisotropy in the $EW_{Ly\alpha}^{obs} \geqslant 30$ Å sample may indicate that this EW threshold is not high enough to produce detectable anisotropy in our mock LAEs. We also find that the mock LAEs with $EW_{Ly\alpha}^{obs} \geqslant 40$ Å show stronger anisotropy in the 1D-CCF along the line of sight than the real LAEs. It may be because O3Es are, on average, located in higher IGM density environments that give higher near-to-far density contrasts. Another intriguing fact is a smaller offset of the 1D-CCF along the line of sight between

the near and far sides seen in Figure 4(d) than the variation of $\langle\delta_F\rangle_{near}^{LOS}$ among O3Es seen in Figure 3. It implies that this selection effect is detectable only statistically.

*4.3. Possible Impacts of Lyα Profile Shape and Peculiar Motion on LAE Selection*

Here we briefly discuss the possible impacts of Lyα profile shape and peculiar motion on the selection of mock LAEs. Changing the blue peak's width (currently $200 \, \text{km s}^{-1}$) and position ($-200 \, \text{km s}^{-1}$) will select a different set of mock LAEs because of a change in the distance range over which Lyα photons are attenuated. The IGM attenuation is sensitive to the fraction of the blue ($<\lambda(Ly\alpha)$) part (24% is assumed). Galaxies with an expanding H I shell (e.g., Verhamme et al. 2008) will have low blue fractions because of systematic redshifting of the entire Lyα profile. As an extreme case, if galaxies have no blue part as found for some LAEs (e.g., Rakic et al. 2011; Hashimoto et al. 2013, 2015), no IGM attenuation, and hence no selection effect, will occur. Galaxies with higher receding peculiar velocities than the IGM will suffer weaker selection effects because of decreased fractions of the Lyα emission subject to the IGM attenuation. If the actual selection effect by the IGM attenuation is much weaker than assumed in our toy model, we have to invoke an alternative mechanism as the origin of the observed anisotropy.

5. Discussion and Summary

We have investigated the IGM H I density traced by Lyα forest absorption around three galaxy populations at $z \sim 2$, particularly paying attention to LAEs. We have found that LAEs show an anisotropic IGM H I density distribution along the line of sight, while continuum-selected galaxies and O3Es do not. Such anisotropy is obtained if LAEs on the far side of dense regions tend not to be selected because of heavier Lyα attenuation by the IGM H I. An examination with mock LAEs supports this idea, finding an anisotropic H I density distribution as observed.

Other mechanisms could also create an anisotropic IGM H I density distribution along the line of sight. One candidate is feedbacks from galaxies. If some feedback energy of a galaxy is emitted toward us, H I gas in front of the galaxy may be swept out or ionized, thus decreasing the IGM H I density on the near side. Quasars and active galactic nuclei (AGNs) jets can drive gas and/or energy in the host galaxies to the surrounding IGM up to distances of a few Mpc (e.g., Perucho et al. 2014; Dabhade et al. 2017, 2020; Momose et al. 2021). Moreover, Hopkins et al. (2020) have indicated that cosmic-ray (CR)-driven outflows extend beyond ~ 1 Mpc. However, none of our LAEs has an AGN signature (Nakajima et al. 2012; Konno et al. 2016; Momose et al. 2021). CR-driven outflows are also unlikely because their effects on the surrounding IGM become negligible at $z \geqslant 1 - 2$ (Hopkins et al. 2020). Thus, feedbacks are unlikely to be the major cause of the anisotropic density distribution around our LAEs.

Taking all these results into account, we conclude that the observed anisotropy of the IGM H I distribution around LAEs is likely due to a selection effect of IGM absorption (Figure 5). If a dense region is viewed from a different direction, some are missed from the original LAE sample, while some are newly selected as if galaxies are playing hide-and-seek using H I gas. We note that anisotropy may also occur along with transverse
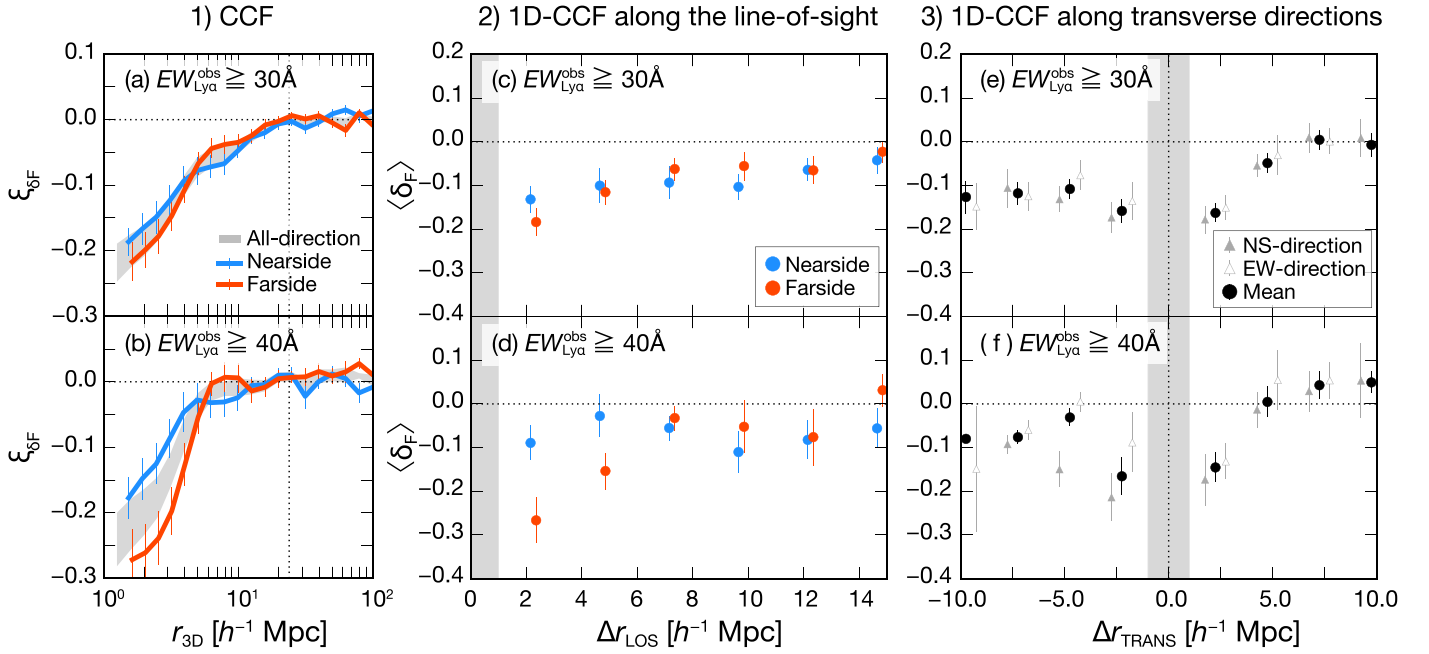
Figure 4. Same as Figure 2, but for mock LAEs, which are O3Es with $EW_{Ly\alpha}^{obs}$ greater than 30 or 40 Å.

directions because of complicated Lyα radiative transfer. Nevertheless, its amplitude seems to be negligible, as we have presented in Sections 3 and 4.2.

Our results also indicate that LAEs may not faithfully trace matter distribution, unlike O3Es and continuum-selected galaxies. Some observational studies have found a 3–15 h^{-1} cMpc offset between the overdensity peaks of LAEs and other galaxy populations (Toshikawa et al. 2016; Shimakawa et al. 2017; Shi et al. 2019). Given the anisotropy of H I density distribution over $r = 3$–5 h^{-1} cMpc found in this study, the discordance reported by those previous studies can be, at least partly, explained by the selection bias. Hence, we should be careful when using LAEs to search for overdensities such as protoclusters.

As has been found in Sections 3 and 4.2, an anisotropic H I density distribution seems to be detectable even when the H I density contrast of a given region is as small as a factor of $\sim$2. Since such a small difference can be easily realized between the densest part and the outskirt of a cosmic filament, we expect an anisotropic distribution across $\sim$10–20 h^{-1} cMpc can be observed if the sightline passes through a filament.

Our finding of an anisotropic H I distribution around LAEs is based on a small sample ($N = 19$). To increase the statistical reliability, a larger sample from a wide-field spectroscopic survey, such as one planned with the Subaru Prime Focus Spectrograph (PFS), is necessary. Follow-up spectroscopy of Lyα emission of the sample galaxies is also useful. Theoretically, there seems to be a debate on the impact of Lyα radiative transfer effects on galaxies in current simulations (e.g., Zheng et al. 2011; Hough et al. 2020). Theoretical studies focusing on line-of-sight dependence of the IGM H I–galaxy connection over a wide range of cosmological environments are also needed.

Appendix
The Density Difference between the Near and Far Sides

The density difference between the near and far sides is evaluated with the fluctuating Gunn–Peterson approximation (FGPA; e.g., Rauch et al. 1997; Croft et al. 1998; Weinberg 1999; Becker et al. 2015). In the FGPA, optical depth, τ_{FGPA}, is described by a power law of normalized gas density, $\rho/\bar{\rho}$, with

$$\tau_{FGPA} \propto \left(\frac{\rho}{\bar{\rho}}\right)^{\beta}. \tag{A1}$$

Then, the density difference is expressed as the ratio

$$\frac{\rho_{far}}{\rho_{near}} = \left(\frac{\tau_{FGPA}^{far}}{\tau_{FGPA}^{near}}\right)^{1/\beta}. \tag{A2}$$

The τ_{FGPA} is calculated from $\langle\delta_F\rangle$ with

$$\tau_{FGPA} = -\ln\left(\frac{F}{\langle F_z\rangle}\right)$$
$$= -\ln(\delta_F + 1). \tag{A3}$$

In this study, we use $\beta = 1.6$ (e.g., Croft et al. 1998; Weinberg 1999) and calculate the H I density difference within $r = 3\,h^{-1}$ cMpc.

We estimate τ_{FGPA}^{far} and τ_{FGPA}^{near} for the 19 real LAEs, and obtain $\rho_{far}/\rho_{near} = 2.1$. Similarly, the mock LAEs satisfying the $EW_{Ly\alpha}^{obs} = 30$ and 35 Å thresholds have $\rho_{far}/\rho_{near} = 1.3$ and 2.1, respectively.
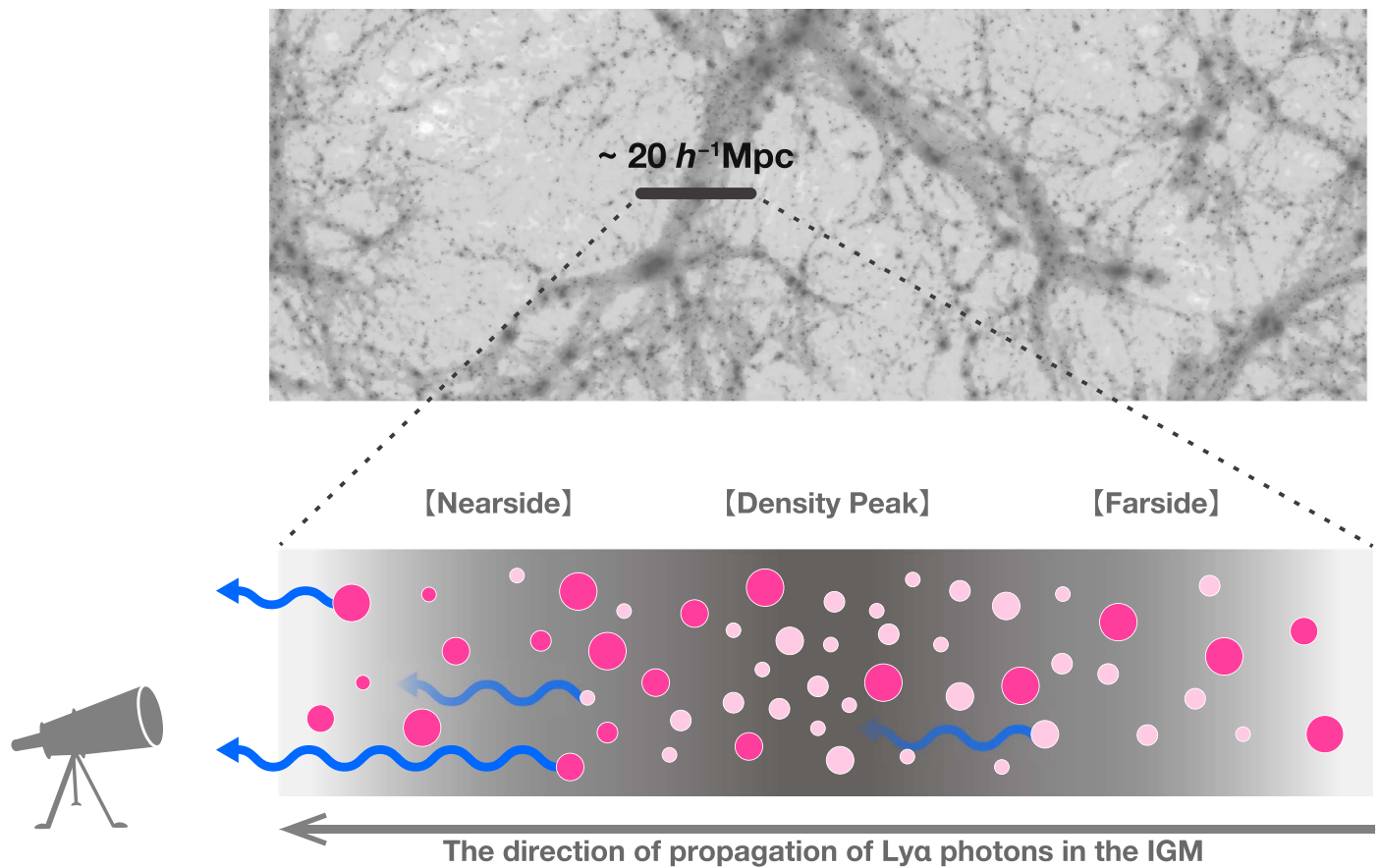
Figure 5. Schematic picture of the selection bias against LAEs in a dense region. The IGM H I density is represented by the grayscale, with darker colors meaning higher densities. Circles indicate galaxies, with larger sizes meaning higher intrinsic Lyα luminosities. The galaxy sample as a whole follows the matter/H I density distribution. It means that the number of galaxies is proportional to the matter/H I density where they are located; the number of galaxies in the darkest area is highest. The Lyα emission from each galaxy travels toward us from right to left in the IGM. Galaxies that are detectable in Lyα are colored in dark pink, while those not are in faint pink. Blue arrows indicate the direction and propagation of Lyα photons in the IGM. The Lyα photons emitted from a galaxy cannot reach us if the IGM H I in $3\ h^{-1}$ cMpc on the near side of the galaxy exceeds a certain density (translucent arrows).

ORCID iDs

Rieko Momose ⓘ https://orcid.org/0000-0002-8857-2905
Kazuhiro Shimasaku ⓘ https://orcid.org/0000-0002-2597-2231
Kentaro Nagamine ⓘ https://orcid.org/0000-0001-7457-8487
Nobunari Kashikawa ⓘ https://orcid.org/0000-0003-3954-4219
Haruka Kusakabe ⓘ https://orcid.org/0000-0002-3801-434X

References

Astropy Collaboration, Robitaille, T. P., Tollerud, E. J., et al. 2013, A&A, 558, A33
Becker, G. D., Bolton, J. S., & Lidz, A. 2015, PASA, 32, e045
Cai, Z., Fan, X., Bian, F., et al. 2017, ApJ, 839, 131
Croft, R. A. C., Weinberg, D. H., Katz, N., & Hernquist, L. 1998, ApJ, 495, 44
Cullen, F., McLure, R. J., Dunlop, J. S., et al. 2020, MNRAS, 495, 1501
Dabhade, P., Gaikwad, M., Bagchi, J., et al. 2017, MNRAS, 469, 2886
Dabhade, P., Röttgering, H. J. A., Bagchi, J., et al. 2020, A&A, 635, A5
de Lapparent, V., Geller, M. J., & Huchra, J. P. 1986, ApJL, 302, L1
Dijkstra, M., Lidz, A., & Wyithe, J. S. B. 2007, MNRAS, 377, 1175
Faucher-Giguère, C.-A., Prochaska, J. X., Lidz, A., Hernquist, L., & Zaldarriaga, M. 2008, ApJ, 681, 831
Gurung-López, S., Orsi, ÁA., Bonoli, S., et al. 2020, MNRAS, 491, 3266
Guzzo, L., Scodeggio, M., Garilli, B., et al. 2014, A&A, 566, A108
Hashimoto, T., Ouchi, M., Shimasaku, K., et al. 2013, ApJ, 765, 70
Hashimoto, T., Verhamme, A., Ouchi, M., et al. 2015, ApJ, 812, 157
Hayes, M. J., Runnholm, A., Gronke, M., & Scarlata, C. 2021, ApJ, 908, 36
Hopkins, P. F., Chan, T. K., Ji, S., et al. 2020, MNRAS, 501, 3640
Hough, T., Gurung-López, S., Orsi, Á., et al. 2020, MNRAS, 499, 2104
Hu, E. M., Cowie, L. L., & McMahon, R. G. 1998, ApJL, 502, L99
Konno, A., Ouchi, M., Nakajima, K., et al. 2016, ApJ, 823, 20
Kusakabe, H., Shimasaku, K., Nakajima, K., & Ouchi, M. 2015, ApJL, 800, L29
Laursen, P., Sommer-Larsen, J., & Razoumov, A. O. 2011, ApJ, 728, 52
Lee, K.-G., Hennawi, J. F., White, M., et al. 2016, ApJ, 817, 160
Lee, K.-G., Krolewski, A., White, M., et al. 2018, ApJS, 237, 31
Libeskind, N. I., van de Weygaert, R., Cautun, M., et al. 2018, MNRAS, 473, 1195
Malhotra, S., & Rhoads, J. E. 2004, ApJL, 617, L5
Matthee, J., Sobral, D., Hayes, M., et al. 2021, arXiv:2102.07779
Momose, R., Shimasaku, K., Kashikawa, N., et al. 2021, ApJ, 909, 117
Nakajima, K., & Ouchi, M. 2014, MNRAS, 442, 900
Nakajima, K., Ouchi, M., Shimasaku, K., et al. 2012, ApJ, 745, 12
Nakajima, K., Ouchi, M., Shimasaku, K., et al. 2013, ApJ, 769, 3
Oke, J. B., Cohen, J. G., Carr, M., et al. 1995, PASP, 107, 375
Oteo, I., Ivison, R. J., Dunne, L., et al. 2018, ApJ, 856, 72
Overzier, R. A., Bouwens, R. J., Cross, N. J. G., et al. 2008, ApJ, 673, 143
Perucho, M., Martí, J.-M., Quilis, V., & Ricciardelli, E. 2014, MNRAS, 445, 1462
Rakic, O., Schaye, J., Steidel, C. C., & Rudie, G. C. 2011, MNRAS, 414, 3265
Rauch, M., Miralda-Escudé, J., Sargent, W. L. W., et al. 1997, ApJ, 489, 7
Shi, K., Huang, Y., Lee, K.-S., et al. 2019, ApJ, 879, 9
Shibuya, T., Ouchi, M., Konno, A., et al. 2018, PASJ, 70, S14
Shibuya, T., Ouchi, M., Nakajima, K., et al. 2014, ApJ, 788, 74
Shimakawa, R., Kodama, T., Hayashi, M., et al. 2017, MNRAS, 468, L21
Shimasaku, K., Hayashino, T., Matsuda, Y., et al. 2004, ApJL, 605, L93
Shimasaku, K., Ouchi, M., Okamura, S., et al. 2003, ApJL, 586, L111
Sobral, D., Matthee, J., Darvish, B., et al. 2018, MNRAS, 477, 2817
Stark, D. P., Ellis, R. S., Chiu, K., Ouchi, M., & Bunker, A. 2010, MNRAS, 408, 1628

Steidel, C. C., Shapley, A. E., Pettini, M., et al. 2004, ApJ, 604, 534
Straatman, C. M. S., Spitler, L. R., Quadri, R. F., et al. 2016, ApJ, 830, 51
Tegmark, M., Blanton, M. R., Strauss, M. A., et al. 2004, ApJ, 606, 702
Toshikawa, J., Kashikawa, N., Overzier, R., et al. 2016, ApJ, 826, 114
Verhamme, A., Schaerer, D., Atek, H., & Tapken, C. 2008, A&A, 491, 89

Wardlow, J. L., Malhotra, S., Zheng, Z., et al. 2014, ApJ, 787, 9
Weinberg, D. E. 1999, in Evolution of Large Scale Structure: From
    Recombination to Garching, ed. A. J. Banday, R. K. Sheth, &
    L. N. da Costa (Garching: ESO), 346
Zheng, Z., Cen, R., Trac, H., & Miralda-Escudé, J. 2011, ApJ, 726, 38